Published in final edited form as:

Clin Oral Implants Res. 2020 November ; 31(11): 1125–1137. doi:10.1111/clr.13659.

Bone formation around unstable implants is enhanced by a WNT protein therapeutic in a preclinical *in vivo* model

Benjamin R. Coyac[1], **Brian Leahy**[1], **Zhijun Li**[1], **Giuseppe Salvi**[1], **Xing Yin**[1], **John B. Brunski**[1], **Jill A. Helms**[1,§]

[1]Department of Plastic and Reconstructive Surgery, School of Medicine, Stanford University, Palo Alto, California 94304, United States of America

Abstract

Objectives: Our objective was to test the hypothesis that local delivery of a WNT protein therapeutic would support osseointegration of an unstable implant placed into an oversized osteotomy and subjected to functional loading.

Materials and Methods: Using a split-mouth design in an ovariectomized (OVX) rat model, 50 titanium implants were placed in oversized osteotomies. Implants were subjected to functional loading. One-half of the implants were treated with a liposomal formulation of WNT3A protein (L-WNT3A); the other half received an identical liposomal formulation containing phosphate buffered saline (PBS). Finite element modeling estimated peri-implant strains caused by functional loading. Histological, molecular, cellular, and quantitative micro-computed tomographic (μCT) imaging analyses were performed on samples from post-implant days (PID) 3, 7, and 14. Lateral implant stability was quantified at PID7 and 14.

Results: Finite element analyses predicted levels of peri-implant strains incompatible with new bone formation. Micro-CT imaging, histological, and quantitative immunohistochemical (IHC) analyses confirmed that PBS-treated implants underwent fibrous encapsulation. In those cases where the peri-implant environment was treated with L-WNT3A, μCT imaging, histological, and quantitative IHC analyses demonstrated a significant increase in expression of proliferative (PCNA) and osteogenic (Runx2, Osterix) markers. One week after L-WNT3A treatment, new bone formation was evident and two weeks later, L-WNT3A treated gaps had a stiffer interface compared to PBS-treated gaps.

Conclusion: In a rat model, unstable implants undergo fibrous encapsulation. If the same unstable implants are treated with L-WNT3A at the time of placement, then it results in significantly more peri-implant bone and greater interfacial stiffness.

[§]Corresponding author: Jill A. Helms, Stanford University, 1651 Page Mill Road, Palo Alto, CA 94304, USA. Phone number: +1 650 736 3640. jhelms@stanford.edu.

Authors' contributions

Study design: BRC, JAH and JBB. Study conduct: BRC. Data collection: BRC, JBB, BL, ZL, XY, GS. Data analysis: BRC, JBB and JAH. Data interpretation: BRC, JBB and JAH. Drafting manuscript: BRC, JBB and JAH. Revising manuscript content: BRC, BL, ZL, XY, GS, JBB and JAH. Approving final version of manuscript: BRC, BL, ZL, XY, GS, JBB and JAH. JBB and JAH take responsibility for the integrity of the data analysis.

Conflict of Interest Statement

All authors declare that no conflict of interest exists.

Keywords

implant failure; osseointegration; stability; dental; oral

Introduction

Micromotion can be detrimental to implant osseointegration (Choi, Ogilvie, Thompson, Miclau, & Helms, 2004). Some degree of micromotion, however, can be beneficial (Goodman & Aspenberg, 1993). The challenge for clinicians is discerning what degree of micromotion is advantageous in stimulating new bone formation, and at what point micromotion becomes disadvantageous.

Clinical evidence conclusively demonstrates that loading an unstable implant will cause it to fail (Monje, Ravida, Wang, Helms, & Brunski, 2019). The current understanding for this failure is that loading causes the implant to move, which in turn creates large interfacial strains that directly interfere with osteogenesis (Perren, 1980). The magnitude of the peri-implant strains is a function of the stiffness of the peri-implant tissue. For example, if the interfacial tissue is rigid, e.g., mineralized bone tissue, then for a given force the resulting peri-implant strains will be relatively low (Perren, 1980) and implants will reliably osseointegrate (Albrektsson, Branemark, Hansson, & Lindstrom, 1981; Skalak, 1986). If, on the other hand, the interfacial tissue is pliable, e.g., a fibrin clot or soft tissue, then the same given force will create relatively large strains, and implants will fail (Martinez, Davarpanah, Missika, Celletti, & Lazzara, 2001; Sagara, Akagawa, Nikai, & Tsuru, 1993). This latter condition is modeled in the clinic and in the laboratory, when implants are either intentionally or inadvertently placed into oversized osteotomies. Even when such implants are positioned subgingivally, they still tend to undergo fibrous encapsulation rather than osseointegration (Friberg, Jemt, & Lekholm, 1991; Yin et al., 2016). Peri-implant strains clearly play a critical role in whether an implant will osseointegrate or not, and the magnitude of those strains is directly related to the stiffness of the bone/implant interface.

Biological factors also influence whether an implant will osseointegrate. In addition to patient risk factors/indicators such as smoking and periodontal disease, local factors also play a role. For example, a gap-interface in dense, Type I bone is more problematic than a similar gap-interface in porous, Type III bone (Li et al., 2017). This difference in whether the implant will osseointegrate is related in some way to the regenerative capacity of the two Types of bone. Compared to Type I bone, Type III bone harbors significantly more stem/osteoprogenitor cells (Li et al., 2017), that are associated with the vascular spaces (Stegen & Carmeliet, 2018).

We hypothesized that stimulating osteoprogenitor cells around a loaded implant in an oversized osteotomy is sufficient to ensure osseointegration, even if a gap interface exists. The underlying reasoning behind this hypothesis was that if osteoprogenitor cells could be activated to differentiate, they would increase the rate of new bone formation in the gap. This, in turn, would stiffen peri-implant tissues and thus reduce the strains associated with functional loading.

As an osteogenic stimulus, we used a liposomal formulation of Wnt3a protein (L-WNT3A). WNTs are potent, pro-osteogenic proteins that accelerate bone formation *via* a Runx2-dependent pathway (Baron & Kneissel, 2013). WNTs also repress bone resorption via a RANKL-dependent mechanism. Together, these two effects culminate in faster new bone formation in multiple preclinical models (Yin et al., 2016; Yuan et al., 2018). Here, we tested in a rat model whether delivery of L-WNT3A was sufficient to ensure osseointegration of functionally loaded implants placed into oversized osteotomies.

Materials & Methods

Animals and experimental plan

Stanford APLAC approved all procedures (#13146), which conform to ARRIVE guidelines. In total, twenty-five 5-week-old female Sprague-Dawley rats (Charles River Laboratories, Wilmington, MA) were used in this study (see flow chart, Supplemental Fig. 1). After one week of acclimation, 6-week-old rats underwent ovariectomy (OVX) and maxillary first molar (mxM1) tooth extraction. General anesthesia was administered via intraperitoneal injection of Ketamine (68mg/kg) and Xylazine (6.8mg/kg); analgesia was provided via subcutaneous injection of Buprenorphine-SR (0.5mg/kg). In addition, a genetic mouse model was used to identify the local distribution of WNT-responsive cells in a similar oral implant procedure. $Axin2^{CreERT2/+}$;$R26R^{mTmG/+}$ male mice aged 3 to 5-months-old were purchased from Jackson Laboratories and underwent an oral implant procedure. To induce Cre expression, tamoxifen (4 mg/25 g body weight) was delivered *via* intraperitoneal injection and animals were then sacrificed at PID3.

Ovariectomy and tooth extraction

The average patient receiving a dental implant is >50 years old, when epidemiological data indicate individuals develop osteopenia and osteoporosis (Cummings & Melton, 2002). To align our experimental model with this demographic characteristic, female rats underwent OVX. In brief, a dorsal midline incision was made between the mid-back and tail base. The peritoneal cavity was accessed through bilateral muscle layer incisions, the ovary was identified, the connection between the fallopian tube and the uterine horn was suture-ligated. After removal of bilateral ovary, the wounds were closed layer by layer (Kalu, 1991).

During the same operation, maxillary first molars (mxM1s) were extracted bilaterally using curved forceps. Bleeding was controlled by local compression. All sites healed without incident.

Osteotomy preparation, implant placement, and L-PBS or L-WNT3A treatment

Six weeks after OVX and mxM1 extraction, rats underwent osteotomy site preparation and implant placement. Under general anesthesia, a full thickness periosteal flap was elevated at the healed mxM1 site. Using a dental handpiece (KaVo Dental, Biberach an der Riss, Germany), a pilot hole (0.33mm) was produced at 1000rpm with saline irrigation, followed by a second drill with a diameter of 0.65mm, produced at 1000rpm with saline irrigation (Table 1). Each osteotomy was made with a fresh drill (Table 1).

In those cases where implants were treated with a liposomal formulation of WNT3A protein (L-WNT3A) or an identical liposomal formulation containing phosphate buffered saline (L-PBS), a split-mouth design was employed. Each of two treatments were randomly assigned to either the right or left halves of the dentition. In all cases, a ~20μL volume of the relevant solution was injected into the osteotomy.

Titanium implants (0.62 mm external diameter, titanium-6 Aluminium-4 Vanadium alloy "Retopins"; NTI, Kahla, Germany) were then placed into the osteotomies by hand, without irrigation. All implants were placed at the level of the occlusal plane. After implant placement, the periosteal flap was repositioned to achieve closure.

After surgery, rats recovered in a controlled, heated environment and were housed in groups of two. Weight changes were <10%. No adverse events (e.g., uncontrolled pain, infection, prolonged inflammation) were encountered.

L-WNT3A and L-PBS preparation and delivery

Liposomal WNT3A (L-WNT3A) was produced as described previously (Dhamdhere et al., 2014). To prepare the L-WNT3A in a collagen gel (Yuan et al., 2018), the following steps were taken: first, a 1.7 mL Eppendorf tube and pipette tips were cooled on ice. After 15 minutes equilibration, the reagents listed in Table 2 were added: a total of 250μL of the type I rat tail collagen (Sigma-Aldrich, St. Louis, MO) was mixed by gentle up and down pipetting, then centrifuged at 12.000 rpm, 4°C, for 10 minutes. Thereafter, supernatant was removed and 250μL of L-WNT3A was added to the solution that was kept on ice. Following gentle pipetting, 20μL of the resulting L-WNT3A/collagen gel was transferred to the osteotomy site. The viscosity of the collagen gel changes from a liquid to a gel-like state at 37°C, and thus stays within the osteotomy site. L-WNT3A-releasing and activity assay were performed. To test the release of L-WNT3A from collagen gel, 100μL of L-WNT3A and type I collagen mixture was placed onto a well of a 96-well plate then incubated at 37°C. After the gel solidified (~20 minutes), 5×10^4 LSL cells were seeded onto the gel (LSL cells are stably transfected with a Wnt-responsive luciferase reporter plasmid pSuperTOPFlash (Addgene, Watertown, MA) and a constitutive LacZ expression construct pEF/Myc/His/LacZ (Invitrogen, Waltham, MA)). Cells were cultured on the L-WNT3A/collagen gel in a CO_2 incubator at 37°C for 18 hours; thereafter, luciferase and β-galactosidase expression levels were quantified using a dual-light combined reporter gene assay system (Applied Biosystems, Waltham, MA) and bioluminescence was measured with triplicate reads on a dual-light ready luminometer (Berthold, Baden-Württemberg, Germany).

Tissue collection and processing

After euthanasia, the entire maxillae of rats were dissected to isolate the region of interest and processed as indicated in Supplemental Table 1. Tissues were collected at post-implant placement day 3 (PID3) to evaluate cell proliferation and osteogenic protein expression instigated in response to L-WNT3A; at PID7 when new bone formation initiates; and at PID 14 to evaluate new bone formation and interfacial stiffness.

Micro-computed tomography (μCT)

Scanning and analyses followed published guidelines (Bouxsein et al., 2010). Three-dimensional μCT imaging was performed at various times after surgery before decalcification of the samples and implant removal. A μCT data-acquisition system (VivaCT 40, Scanco, Brüttisellen, Switzerland) at 10.5μm voxel size (70kV, 115μA, 300ms integration time) was used for scanning and reconstruction. Bone morphometry was performed using the acquisition system's analysis software. Multiplanar reconstruction and volume rendering were carried out using Avizo (FEI, Hillsboro, OR) and ImageJ (NIH, Bethesda, MD) software. Images were organized using Adobe Photoshop and Illustrator (Adobe, San Jose, CA).

Histology

For Aniline blue staining, slides were treated with a saturated solution of picric acid, followed by a 5% Phosphotungstic acid solution and stained in 1% Aniline blue. Pentachrome staining was performed as described (Movat, 1955). In brief, after dehydration, slides were stained with 1% Alcian Blue (#A5268, Sigma-Aldrich, St. Louis, MO), Verhoeffs Hematoxylin (#S71299, Fisher Scientific, Pittsburg, PA), Sodium Thiosulfate (#14518, Alfa Aesar, Haverhill, MA), Crocein-Scarlet-Acid Fuchsin solution (#22914, Chem Impex International, Wood Dale, IL; #F8129, Sigma-Aldrich, St. Louis, MO), 5% Phosphotungstic Acid (#P4006, Sigma-Aldrich, St. Louis, MO) and Saffron, washing steps between each stain used ethanol, acetic acid and distilled water. Slides were then dehydrated and mounted using Permount (Fisher Scientific, Pittsburg, PA). Pentachrome-stained tissues reveal nuclei as blue to black color, cytoplasm stains red, collagen stains yellow to greenish yellow, and fibrous tissue stains an intense red. For Picrosirius Red staining, slides were stained with picrosirius solution (0.5 g Sirius red, #35780, Pfaltz & Bauer, Waterbury, CT) dissolved in 500 mL saturated picric acid solution and then viewed under polarized light.

Immunostaining

Immunostaining was performed using standard procedures (Yuan et al., 2018). Following de-paraffinization, tissue sections were permeabilized with 0.5% TritonX-100. After antigen retrieval, slides were blocked with 5% goat serum (Vector Laboratories, Burlingame, CA) for 1h at room temperature and incubated with primary antibodies overnight at 4°C. After washing with PBS, slides were incubated with Cyanine5 conjugated goat anti-rabbit secondary antibody (A10523, Invitrogen, Waltham, MA) for 30 minutes, then mounted with DAPI mounting medium (Vector Laboratories, Burlingame, CA). The primary antibodies used in this study are: anti-Runx2 (1:1000; ab192256, Abcam, Cambridge, MA), anti-PCNA (1:10000, ab18197, Abcam, Cambridge, MA), anti-Osterix (1:100; ab22552, Abcam, Cambridge, MA), anti-Vimentin (1:100; 5741, Cell Signaling Technology, Danvers, MA), anti-Collagen I (1:500; ab34710, Abcam, Cambridge, MA), anti-GFP (1:500; 2956T, Cell Signaling Technology, Danvers, MA).

Histomorphometric analyses

Histomorphometric measurements were performed using ImageJ software (NIH, Bethesda, MD). A minimum of 4 implant sites was analyzed for each time point. For each implant site,

a minimum of three aniline blue-stained histologic sections in the sagittal plane and spanning the distance from the buccal to the palatal aspects of the alveolar plates, were used to quantify both the proportion of bone in contact with the implant surface and the amount of bone in the peri-implant region. Each section was photographed using a Leica digital image system at 20x magnification. To find the ratio of protein expression in the peri-implant region, the number of $PCNA^{+ve}$, $Runx2^{+ve}$ and $Osterix^{+ve}$ cells within the peri-implant region were measured, and divided by the surface in μm^2 in the same peri-implant area (Table 3).

Finite Element Model

Finite element analyses were conducted using COMSOL Multiphysics 5.4. A solid model of a Ti-6Al-4V retopin implant (0.62 mm outer diameter, 0.49 mm inner diameter) was installed in a slightly oversized (i.e., 0.65 mm) drill hole in alveolar bone that was modeled as a simple cylinder of 2 mm diameter and 1.5 mm height. The gap region between the bone and the implant (see Table 1 for measurements) was subdivided into three subdomains to permit strain levels examination at different radial distances from the implant's surface. This also allowed alteration of the mechanical properties in these regions following implantation. The retopin implant was installed in the drill hole to a depth of 1.25 mm. The boundary conditions of the model included fixed constraint of the bottom surface of the cylinder of bone, and application of an axially-downward (negative z-direction) force magnitude of 0.8N on the top surface of the retopin, which simulated the low-end of possible axial forces from masticatory activities in the rat's mouth. There was a no-slip boundary condition between implant and tissue (clot and fibrin) assumed to fill the gap region between the implant and bone. All materials were assumed to be linearly elastic with the following values of Young's modulus and Poisson's ratio, respectively: retopin 400MPa and 0.33; retopin 105GPa and 0.33; blood clot and fibrin 0.28MPa and 0.33. The modulus values for bone were estimated from published literature (Cory et al., 2010) and the BV/TV values for the bone in a healed extraction site in a rat (Chen et al., 2018). The modulus value of 0.28MPa for the clot/fibrin mixture in the gap between implant and bone was estimated from published literature (Munster, Jawerth, Fabry, & Weitz, 2013; Piechocka, Bacabac, Potters, Mackintosh, & Koenderink, 2010). Based on symmetry of the problem, the full 3-D problem was reduced to one-quarter size and solved accordingly. The problem was meshed with 60,786 elements and solved for 255,531 degrees of freedom.

Lateral stability tests

The Lateral Stability Test (LST) was based on an assumed linear relationship between the magnitude of a lateral force (F) exerted at the top of an implant and the resulting lateral displacement of the implant (Δx), i.e., we assumed a spring-like relationship given by the equation $F = k \Delta x$, where k is the lateral stiffness in Newtons per micron (Wang et al., 2017). This test assumed that the titanium implant (of external diameter 0.62 mm) was rigid compared to its interfacial bone under the test conditions, meaning that any implant displacement arose from deformation of interfacial bone. Our experience with the method, including laboratory testing and modeling with FE analysis, indicated that this assumption was valid for displacements in the range of about 0 to 100 μm and for small forces on the order of a few Newtons or less (Wang et al., 2017; Yin et al., 2016).

To carry out a LST, animals were sacrificed followed by removal of the maxillae and sectioning each maxilla in half. Half-maxillae containing the implants were submerged in 100% ethanol then rigidly clamped to a solid support, thereby positioning the implant between a linear actuator (Ultra Motion Digit D-A.083-AB-HT17075-2-K-B/3, Mattituck, NY) equipped with an in-line 10N force transducer (Honeywell Model 31, Charlotte, NC), and a displacement transducer (MG-DVRT-3, Lord MicroStrain, Williston, VT). A tare load of 0.05N was applied to one side of the implant while the stylus of the displacement transducer was positioned on the diametrically-opposite side of the implant. Under software command, the actuator was triggered to deliver 3 cycles of a lateral displacement *vs.* time waveform having a peak displacement of about 30μm. The lateral force required to develop this lateral displacement was measured by the force transducer. The lateral displacement of the implant was applied and measured at a consistent height of ~0.5mm above the crest of the maxillary bone. Lateral force and implant displacement were recorded at 80Hz and stored to disc for later data analysis and calculation of a lateral stiffness k (in Newtons/μm), defined as the ratio between force and displacement.

Statistics

Each animal was controlled with regards to genetics (i.e., rats were inbred), sex, age, weight, overall health status, environment, and bone health, e.g., variables that are known to contribute to clinical differences in implant success (Noguerol, Munoz, Mesa, de Dios Luna, & O'Valle, 2006). Consequently, the implant itself was considered as the random variable and therefore was used as the statistical unit. An online tool, designed for calculating the minimum sample size was employed: https://clincalc.com/stats/SampleSize.aspx. All estimations were performed by setting parameters so that α (type I error)=0.05, β (type II error)=0.2, enrollment ratio=1. Comparison between groups was performed using a paired t-test with the R 3.3.2 software. Results are presented in the form of mean ± standard deviation to summarize the central tendency and dispersion because of the absence of outliers in their distribution. Differences between groups were considered significant when $p < 0.05$ (Table 3).

Results

Modeling fibrous encapsulation in response to immediate loading of an unstable implant

To explore the entire range of responses of peri-implant tissues, we produced a rat model of immediate, functional implant loading. In these experiments, implants purposefully lacked primary stability. To achieve this state, maxillary first molars were extracted, and after complete healing, implants were placed into oversized osteotomies (Fig. 1A).

FE modeling was used to calculate the distribution and magnitude of compressive strains resulting from immediate loading of the implant. The strain state was displayed in two ways (Fig. 1B). In response to loading, 350% strains were concentrated at the thread tips, with lower strains, i.e., <50%, being found between the threads (Fig. 1B, left panel). These same results are also shown in a deformed geometry, where the implant is displaced (compare threads #1 and #2 in both images, Fig. 1B). The flame-shaped pattern of the strain (right

panel, Fig. 1B) illustrated the peri-implant domains that are subjected to higher strains on the order of 350%.

Fourteen days later, histological and immunobiological analyses revealed that fibrous tissue surrounded the implant (Fig. 1C). Picrosirius red staining showed that collagen fibers were aligned parallel to the long axis of the implant (Fig. 1D). Widespread Vimentin immunostaining confirmed that peri-implant cells had differentiated into fibroblasts (Fig. 1E). This finding of fibrous encapsulation in response to high peri-implant strains is in keeping with the published literature showing that strains in excess of 30% are unfavorable for bone formation (Carter, 1987; Wazen et al., 2013).

L-WNT3A treatment can initially overcome an unfavorable mechanical environment

Having demonstrated a correlation between excessive compressive/tensile strains and the fibrous differentiation of peri-implant cells, we next set out to determine whether this cellular fate was malleable. We opted to use the pro-osteogenic growth factor WNT3A, which here was formulated as a liposomal protein therapeutic (Dhamdhere et al., 2014; Zhao et al., 2009). A split-mouth design was used, and peri-implant injections of liposomal WNT3A (L-WNT3A) or a liposomal formulation of phosphate buffered saline (L-PBS) as a control were performed at the time of implant placement (Fig. 2A,B).

We examined the consequences of Wnt pathway activation as a result of treatment, by harvesting samples at PID3 and evaluating the peri-implant tissues. Implants in both cases were surrounded by undifferentiated cells but compared to L-PBS treated controls, L-WNT3A treatment had elicited a significant burst in cell proliferation (Fig. 2C,D; quantified in E). In those implant cases treated with L-WNT3A, expression of the pre-osteogenic transcription factors Runx2 and Osterix were also significantly higher (Fig. 2F,J; quantified in H,K). Specifically, Osterix^{+ve} cells were located between the tips of the implant threads (Fig. 2J), where our FE model predicted that strain and stress were the lowest (Fig. 1B). Together, these data demonstrated that L-WNT3A treatment enhanced cell proliferation and initiated osteogenesis in cells occupying the peri-implant environment around an unstable implant.

In lower strain regions, L-WNT3A enables new peri-implant bone formation

We followed the trajectory of osseointegration. On PID7, 1 week after peri-implant injection of L-WNT3A or L-PBS, sites were evaluated by μCT (Bouxsein et al., 2010). We compared the two groups by defining the peri-implant gap on two-dimensional (2D) μCT sections and compiling the sections into a 3D image so as to distinguish and quantify the amount of bone that had specifically formed in the peri-implant gap. For example, in L-PBS-treated controls, some newly mineralized tissue was detectable in the gap interface (Fig. 3A). In L-WNT3A treated cases, the gap was occupied by significantly more mineralized matrix (Fig. 3B). Whereas some portion of the L-PBS treated gap, i.e., 23% was occupied by bone (Fig. 3C), a greater percentage, i.e., 50% was occupied by bone in the L-WNT3A treated cases (Fig. 3D). The new bone was primarily located between the thread tips (quantified in Fig. 3E) where lower strains exist.

L-WNT3A treated implant cases showed a trend towards better secondary stability as demonstrated by a lateral stability test. A pairwise comparison showed that in all cases (N=9), the L-WNT3A treated implant had a stiffer interface than the contralateral L-PBS treated interface; this analysis, however, did not reach statistical significance (Fig. 3F).

Compared to L-PBS controls, the finding of an experimentally stiffer interface in L-WNT3A treated cases was supported by higher expression of Collagen Type I (Fig. 3G,H). Also compared to controls, where the peri-implant region was occupied by Vimentin-expressing fibroblasts, L-WNT3A treated cases had very low Vimentin expression (Fig. 3I,J).

Although new bone formed in the peri-implant gap of the L-WNT3A treated cases, there was an unexpected pattern to the tissue: compared to the fibrous-encapsulated L-PBS treated controls, the new bone that formed in the L-WNT3A treated cases was disconnected from the edges of the osteotomy (Fig. 3K,L). The bone appeared to have formed first at the implant surface, specifically between the threads, but had not yet fused with the osteotomy edges. Our next studies focused on understanding the reason for this unusual ossification pattern.

A mechanical template dictates the pattern of new peri-implant bone formation

Peri-implant bone formed in an unexpected pattern in response to the L-WNT3A treatment. It was important to note that this peri-implant environment was being subjected to unfavorable strains. For example, FE modeling predicted that strain magnitudes at the thread tips were ~300% (red spots, Fig. 4A) whereas strains between the thread tips were <50% (blue regions, Fig. 4B). At higher magnification, three continuous strain fields were evident: in zone 1, between the implants' threads, strains were predicted to be the lowest; in zone 2, away from the implant surface, strains were ~70%; and in zone 3, at the thread tips, strains were predicted to be the highest, at ~300% (Fig. 4A').

We used FE modeling coupled with molecular and cellular analyses to understand what happened in these three zones in response to L-WNT3A (Fig. 4B). For example, 72h after L-WNT3A treatment, cells primarily in zone 1 upregulated the expression of a direct Wnt target gene, Axin2 (Fig. 4C, schematized in Fig. 4D). Within 4 more days, on PID7, pentachrome staining identified new mineralized matrix (Fig. 4E,F) and by PID14, all peri-implant cells showed evidence of osteogenic differentiation and mineralization, as shown by ALP staining (Fig. 4G,H) and Osterix immunostaining (Fig. 4I). Lateral stability testing confirmed that the L-WNT3A treated cases had a significantly stiffer interface by this timepoint (Fig. 4J).

Discussion

While surgeons studiously avoid producing gap interfaces around implants, we intentionally produced this situation in a laboratory setting in order to mimic the detrimental clinical situation where an implant lacks primary stability and yet is still subjected to masticatory loading (Esposito, Thomsen, Ericson, & Lekholm, 1999). For example, in creating a gap interface around an implant, then immediately allowing that implant to be loaded, we ensured that the implant would become encapsulated in a fibrous envelope (Yin et al., 2016).

This provided us with the unique opportunity to understand in detail the biomechanical basis for this type of failure, and then test if a modification of the biological environment at the time of surgery could overcome the unfavorable mechanical environment. We envisioned that if this biological strategy were effective, it could be routinely employed in cases where either insufficient peri-implant bone exists (Buser, Chappuis, Belser, & Chen, 2017), or in cases where osseointegration success is at risk, such as in immediately loaded implants placed into fresh extraction sockets (Buser et al., 2017).

Exploring the mechanical and molecular basis for implant failure

Implants can fail for multiple reasons. For example, in a previous study we created a situation where an implant was placed into an *undersized* osteotomy. Inserting the implant produced compressive strains that severely damaged the peri-implant bone, resulting in sustained resorption and implant loosening and ultimately, fibrous encapsulation (Coyac et al., 2019). Here, we created a situation where an implant was placed into an *oversized* osteotomy and in this case, immediate loading of the implants was a key to their failure: loading generated high strains in the gap interface (Fig. 1), resulting in an unfavorable environment for osteogenic cell differentiation (Fig. 2). If these same implants were subocclusal, the loading and strains would be decreased, and they would have more chance to successfully osseointegrate (Li et al., 2017).

Since immediately loaded implants placed into gap interfaces fail (Fig. 1), one might legitimately wonder if the “solution” to this detrimental situation is to remove loading from the equation. Clinical data, however, indicate that simply unloading such implants is rarely successful (Sheridan, Decker, Plonka, & Wang, 2016; Vidyasagar & Apse, 2004). One reason for this may be that the initial strain environment drives peri-implant cells to differentiate into fibroblasts (Esposito et al., 1999); even if loading is stopped, the state of fibrous encapsulation persists (Piattelli et al., 2003; Scarano et al., 2007).

Our data demonstrate that the fate of the peri-implant cells can be changed, and this does not appear to be unique to the peri-implant environment. For example, in a study on long bone fracture healing, Kruck and colleagues showed that an unstable fracture – which will not heal if it is simply stabilized – could be induced to do so if stabilization was coupled to systemic delivery of an anti-Sclerostin antibody (SclAb; (Kruck et al., 2018)). If the fracture was not stabilized, then the pro-osteogenic effects of SclAb could not overcome the persistent unfavorable mechanical environment (Kruck et al., 2018). Clearly, these data demonstrate that biological and mechanical factors act synergistically to bring about bone healing, whether in a peri-implant environment or in a fracture callus (Carter, 1987).

SclAb therapy is designed to elevate Wnt signaling (Hoeppner, Secreto, & Westendorf, 2009), and in Kruck’s study as well as in others, SclAb increases new bone formation (Virdi et al., 2015; Witcher et al., 2018; Yu et al., 2018). In these studies, SclAb was delivered systemically, and for the entire period of the experiments (Virdi et al., 2015; Witcher et al., 2018; Yu et al., 2018). In our experiments, L-WNT3A was delivered once, at the time of surgery, and only to the site where new bone formation was required (Fig. 4). This treatment regimen has a number of advantages: first, the osteogenic stimulus is only delivered when and where it is needed, thus avoiding known negative feedback loops that are activated in

response to SclAb therapy (Florio et al., 2016). Second, a single, local delivery for a pro-osteogenic stimulus avoids continuous administration of a drug that appears to be counterproductive to bone remodeling (Koide et al., 2017; Kruck et al., 2018). Third, local delivery of L-WNT3A appears to be a safer option to enhance implant osseointegration, in that it avoids known cardiovascular side effects associated with systemic delivery of SclAb (Novo-Rodriguez et al., 2018; Saag et al., 2017).

Limitations of this study and conclusions

We were not able to confirm complete osseointegration around an unstable implant in the timeframe of this study. Although the peri-implant environment was becoming stiffer over time (Figs. 3,4), and this stiffer interface should decrease strains and support further bone formation, we nonetheless did not see full osseointegration by post-implant day 14 (Fig. 3). There are a number of possible explanations for this: first, we may not have waited a long enough time for osseointegration to have occurred. In previous studies where implants were placed into oversized osteotomies, treated with L-WNT3A but *not* intentionally loaded, fibrous encapsulation was reversed and osseointegration occurred within 21 days.

Another possible explanation for a failure to achieve full osseointegration is that we delivered a single dose of L-WNT3A at the time of implant placement and this may be inadequate. The timing of delivery may also be sub-optimal, since the initial period after implant placement is largely characterized by extensive osteocyte death. From a biological point of view, it may be better to deliver a WNT protein therapeutic during the initial healing period rather than immediately after implant placement.

In a certain set of mechanical conditions shown here, where peri-implant strains were at least 350%, osseointegration was not completed at PID14 (Figs. 3,4). It is formally possible that if the initial peri-implant strains were significantly higher, then we also may not have achieved any peri-implant bone formation, regardless of how long we waited. In future studies we intend to explore longer timepoints with continual occlusal loading to explore the extent to which osseointegration occurs in a detrimental mechanical environment.

Supplementary Material

Refer to Web version on PubMed Central for supplementary material.

Acknowledgements

This work was supported by NIH R01 DE024000-12 to JAH and JBB.

J.A.H. is co-founder of Ankasa Regenerative Therapeutics, Inc., a biopharmaceutical company manufacturing a form of L-WNT3A for commercial use.

References

Albrektsson T, Branemark PI, Hansson HA, & Lindstrom J. (1981). Osseointegrated titanium implants. Requirements for ensuring a long-lasting, direct bone-to-implant anchorage in man. Acta Orthop Scand, 52(2), 155–170. [PubMed: 7246093]

Baron R, & Kneissel M. (2013). WNT signaling in bone homeostasis and disease: from human mutations to treatments. Nat Med, 19(2), 179–192. doi:10.1038/nm.3074 [PubMed: 23389618]

Bouxsein ML, Boyd SK, Christiansen BA, Guldberg RE, Jepsen KJ, & Muller R. (2010). Guidelines for assessment of bone microstructure in rodents using micro-computed tomography. J Bone Miner Res, 25(7), 1468–1486. doi:10.1002/jbmr.141 [PubMed: 20533309]

Buser D, Chappuis V, Belser UC, & Chen S. (2017). Implant placement post extraction in esthetic single tooth sites: when immediate, when early, when late? Periodontol 2000, 73(1), 84–102. doi:10.1111/prd.12170 [PubMed: 28000278]

Carter DR (1987). Mechanical loading history and skeletal biology. J Biomech, 20(11–12), 1095–1109. [PubMed: 3323201]

Chen CH, Wang L, Serdar Tulu U, Arioka M, Moghim MM, Salmon B, . . . Helms JA (2018). An osteopenic/osteoporotic phenotype delays alveolar bone repair. Bone, 112, 212–219. doi:10.1016/j.bone.2018.04.019 [PubMed: 29704698]

Choi P, Ogilvie C, Thompson Z, Miclau T, & Helms JA (2004). Cellular and molecular characterization of a murine non-union model. J Orthop Res, 22(5), 1100–1107. [PubMed: 15304285]

Cory E, Nazarian A, Entezari V, Vartanians V, Muller R, & Snyder BD (2010). Compressive axial mechanical properties of rat bone as functions of bone volume fraction, apparent density and micro-ct based mineral density. J Biomech, 43(5), 953–960. doi:10.1016/j.jbiomech.2009.10.047 [PubMed: 20003979]

Coyac BR, Leahy B, Salvi G, Hoffmann W, Brunski JB, & Helms JA (2019). A preclinical model links osseo-densification due to misfit and osseo-destruction due to stress/strain. Clin Oral Implants Res. doi:10.1111/clr.13537

Cummings SR, & Melton LJ (2002). Epidemiology and outcomes of osteoporotic fractures. Lancet, 359(9319), 1761–1767. doi:10.1016/S0140-6736(02)08657-9 [PubMed: 12049882]

Dhamdhere GR, Fang MY, Jiang J, Lee K, Cheng D, Olveda RC, . . . Helms JA (2014). Drugging a stem cell compartment using Wnt3a protein as a therapeutic. PLoS ONE, 9(1), e83650. doi:10.1371/journal.pone.0083650 [PubMed: 24400074]

Esposito M, Thomsen P, Ericson LE, & Lekholm U. (1999). Histopathologic observations on early oral implant failures. Int J Oral Maxillofac Implants, 14(6), 798–810. [PubMed: 10612916]

Florio M, Gunasekaran K, Stolina M, Li X, Liu L, Tipton B, . . . Ominsky MS (2016). A bispecific antibody targeting sclerostin and DKK-1 promotes bone mass accrual and fracture repair. Nat Commun, 7, 11505. doi:10.1038/ncomms11505 [PubMed: 27230681]

Friberg B, Jemt T, & Lekholm U. (1991). Early failures in 4,641 consecutively placed Branemark dental implants: a study from stage 1 surgery to the connection of completed prostheses. Int J Oral Maxillofac Implants, 6(2), 142–146. [PubMed: 1809668]

Goodman S, & Aspenberg P. (1993). Effects of mechanical stimulation on the differentiation of hard tissues. Biomaterials, 14(8), 563–569. [PubMed: 8399946]

Hoeppner LH, Secreto FJ, & Westendorf JJ (2009). Wnt signaling as a therapeutic target for bone diseases. Expert Opin Ther Targets, 13(4), 485–496. [PubMed: 19335070]

Kalu DN (1991). The ovariectomized rat model of postmenopausal bone loss. Bone Miner, 15(3), 175–191. [PubMed: 1773131]

Koide M, Kobayashi Y, Yamashita T, Uehara S, Nakamura M, Hiraoka BY, . . . Udagawa N. (2017). Bone Formation Is Coupled to Resorption Via Suppression of Sclerostin Expression by Osteoclasts. J Bone Miner Res, 32(10), 2074–2086. doi:10.1002/jbmr.3175 [PubMed: 28543818]

Kruck B, Zimmermann EA, Damerow S, Figge C, Julien C, Wulsten D, . . . Willie BM (2018). Sclerostin Neutralizing Antibody Treatment Enhances Bone Formation but Does Not Rescue Mechanically Induced Delayed Healing. J Bone Miner Res, 33(9), 1686–1697. doi:10.1002/jbmr.3454 [PubMed: 29694687]

Li J, Yin X, Huang L, Mouraret S, Brunski JB, Cordova L, . . . Helms JA (2017). Relationships among Bone Quality, Implant Osseointegration, and Wnt Signaling. J Dent Res, 96(7), 822–831. doi:10.1177/0022034517700131 [PubMed: 28571512]

Martinez H, Davarpanah M, Missika P, Celletti R, & Lazzara R. (2001). Optimal implant stabilization in low density bone. Clin Oral Implants Res, 12(5), 423–432. [PubMed: 11564101]

Monje A, Ravida A, Wang HL, Helms JA, & Brunski JB (2019). Relationship Between Primary/Mechanical and Secondary/Biological Implant Stability. Int J Oral Maxillofac Implants, 34, s7–s23. doi:10.11607/jomi.19suppl.g1 [PubMed: 31116830]

Movat HZ (1955). Demonstration of all connective tissue elements in a single section; pentachrome stains. AMA Arch Pathol, 60(3), 289–295. [PubMed: 13248341]

Munster S, Jawerth LM, Fabry B, & Weitz DA (2013). Structure and mechanics of fibrin clots formed under mechanical perturbation. J Thromb Haemost, 11(3), 557–560. doi:10.1111/jth.12123 [PubMed: 23489915]

Novo-Rodriguez C, Garcia-Fontana B, Luna-Del Castillo JD, Andujar-Vera F, Avila-Rubio V, Garcia-Fontana C, . . . Munoz-Torres M. (2018). Circulating levels of sclerostin are associated with cardiovascular mortality. PLoS ONE, 13(6), e0199504. doi:10.1371/journal.pone.0199504 [PubMed: 29928063]

Perren SM, Cordey J. (1980). The Concept of Interfragmentary Strain In HK IU (Ed.), Current Concepts of Internal Fixation of Fractures. (pp. 63–77). New York: Springer-Verlag.

Piattelli A, Scarano A, Favero L, Iezzi G, Petrone G, & Favero GA (2003). Clinical and histologic aspects of dental implants removed due to mobility. J Periodontol, 74(3), 385–390. doi:10.1902/jop.2003.74.3.385 [PubMed: 12710760]

Piechocka IK, Bacabac RG, Potters M, Mackintosh FC, & Koenderink GH (2010). Structural hierarchy governs fibrin gel mechanics. Biophys J, 98(10), 2281–2289. doi:10.1016/j.bpj.2010.01.040 [PubMed: 20483337]

Saag KG, Petersen J, Brandi ML, Karaplis AC, Lorentzon M, Thomas T, . . . Grauer A. (2017). Romosozumab or Alendronate for Fracture Prevention in Women with Osteoporosis. N Engl J Med, 377(15), 1417–1427. doi:10.1056/NEJMoa1708322 [PubMed: 28892457]

Sagara M, Akagawa Y, Nikai H, & Tsuru H. (1993). The effects of early occlusal loading on one-stage titanium alloy implants in beagle dogs: a pilot study. J Prosthet Dent, 69(3), 281–288. [PubMed: 8445559]

Scarano A, Carinci F, Quaranta A, Iezzi G, Piattelli M, & Piattelli A. (2007). Correlation between implant stability quotient (ISQ) with clinical and histological aspects of dental implants removed for mobility. Int J Immunopathol Pharmacol, 20(1 Suppl 1), 33–36. [PubMed: 17897499]

Sheridan RA, Decker AM, Plonka AB, & Wang HL (2016). The Role of Occlusion in Implant Therapy: A Comprehensive Updated Review. Implant Dent, 25(6), 829–838. doi:10.1097/ID.0000000000000488 [PubMed: 27749518]

Skalak R. (1986). Osseointegration biomechanics. J Oral Implantol, 12(3), 350–356. [PubMed: 3470523]

Stegen S, & Carmeliet G. (2018). The skeletal vascular system - Breathing life into bone tissue. Bone, 115, 50–58. doi:10.1016/j.bone.2017.08.022 [PubMed: 28844835]

Vidyasagar L, & Apse P. (2004). Dental Implant Design and Biological Effects on Bone-Implant Interface. Stomatologija, Baltic Dental and Maxillofacial Journal, 6, 51–54.

Virdi AS, Irish J, Sena K, Liu M, Ke HZ, McNulty MA, & Sumner DR (2015). Sclerostin antibody treatment improves implant fixation in a model of severe osteoporosis. J Bone Joint Surg Am, 97(2), 133–140. doi:10.2106/JBJS.N.00654 [PubMed: 25609440]

Wang L, Wu Y, Perez KC, Hyman S, Brunski JB, Tulu U, . . . Helms JA (2017). Effects of Condensation on Peri-implant Bone Density and Remodeling. J Dent Res, 96(4), 413–420. doi:10.1177/0022034516683932 [PubMed: 28048963]

Wazen RM, Currey JA, Guo H, Brunski JB, Helms JA, & Nanci A. (2013). Micromotion-induced strain fields influence early stages of repair at bone-implant interfaces. Acta Biomater, 9(5), 6663–6674. doi:10.1016/j.actbio.2013.01.014 [PubMed: 23337705]

Witcher PC, Miner SE, Horan DJ, Bullock WA, Lim KE, Kang KS, . . . Robling AG (2018). Sclerostin neutralization unleashes the osteoanabolic effects of Dkk1 inhibition. JCI Insight, 3(11). doi:10.1172/jci.insight.98673

Yin X, Li J, Chen T, Mouraret S, Dhamdhere G, Brunski JB, . . . Helms JA (2016). Rescuing failed oral implants via Wnt activation. J Clin Periodontol, 43(2), 180–192. doi:10.1111/jcpe.12503 [PubMed: 26718012]

Yu SH, Hao J, Fretwurst T, Liu M, Kostenuik P, Giannobile WV, & Jin Q. (2018). Sclerostin-Neutralizing Antibody Enhances Bone Regeneration Around Oral Implants. Tissue Eng Part A, 24(21–22), 1672–1679. doi:10.1089/ten.TEA.2018.0013 [PubMed: 29921173]

Yuan X, Pei X, Zhao Y, Tulu US, Liu B, & Helms JA (2018). A Wnt-Responsive PDL Population Effectuates Extraction Socket Healing. J Dent Res, 22034518755719. doi:10.1177/0022034518755719

Zhao L, Rooker SM, Morrell N, Leucht P, Simanovskii D, & Helms JA (2009). Controlling the in vivo activity of Wnt liposomes. Methods Enzymol, 465, 331–347. doi:10.1016/S0076-6879(09)65017-5 [PubMed: 19913175]

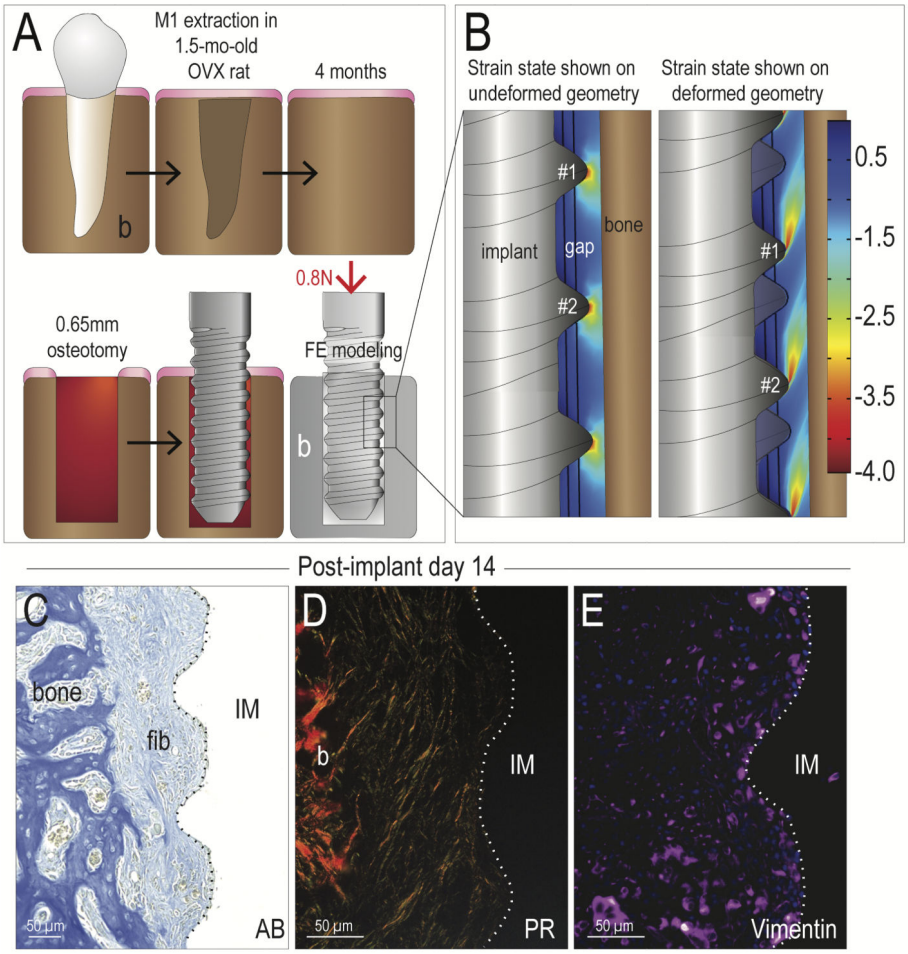

Fig. 1. Peri-implant cells become fibroblasts in regions with high tensile and compressive strains.

(A) Schematic of the experimental design, where an OVX surgery was performed and maxillary first molars were extracted within a single surgical procedure. After a 6-week healing period, an osteotomy was prepared in the healed M1 site, followed by placement of an implant. The osteotomy was oversized relative to the diameter of the implant (see Table 1). The implant was positioned at the level of the occlusal plane, resulting in immediate loading. FE modeling of this situation was performed, where (B) a compressive strain maps was generated, which illustrated that principal strain magnitudes around the implant thread tips were ~350% and <50% between the thread tips. The left panel illustrated the strain distribution super-imposed on the implant in the undeformed geometry, where the right panel illustrated the same strains in the deformed geometry. On PID14, fibrous tissue encapsulation was visualized by (C) aniline blue histology, (D) picrosirius red staining, viewed under polarized light; and (E) immunostaining for the fibrotic tissue marker Vimentin. Abbreviations: AB, Aniline blue; PR, Picrosirius red; b, bone; fib, fibrous tissue; M1, maxillary first molar; IM, implant; OVX, ovariectomy. Scale bars = 50µm.

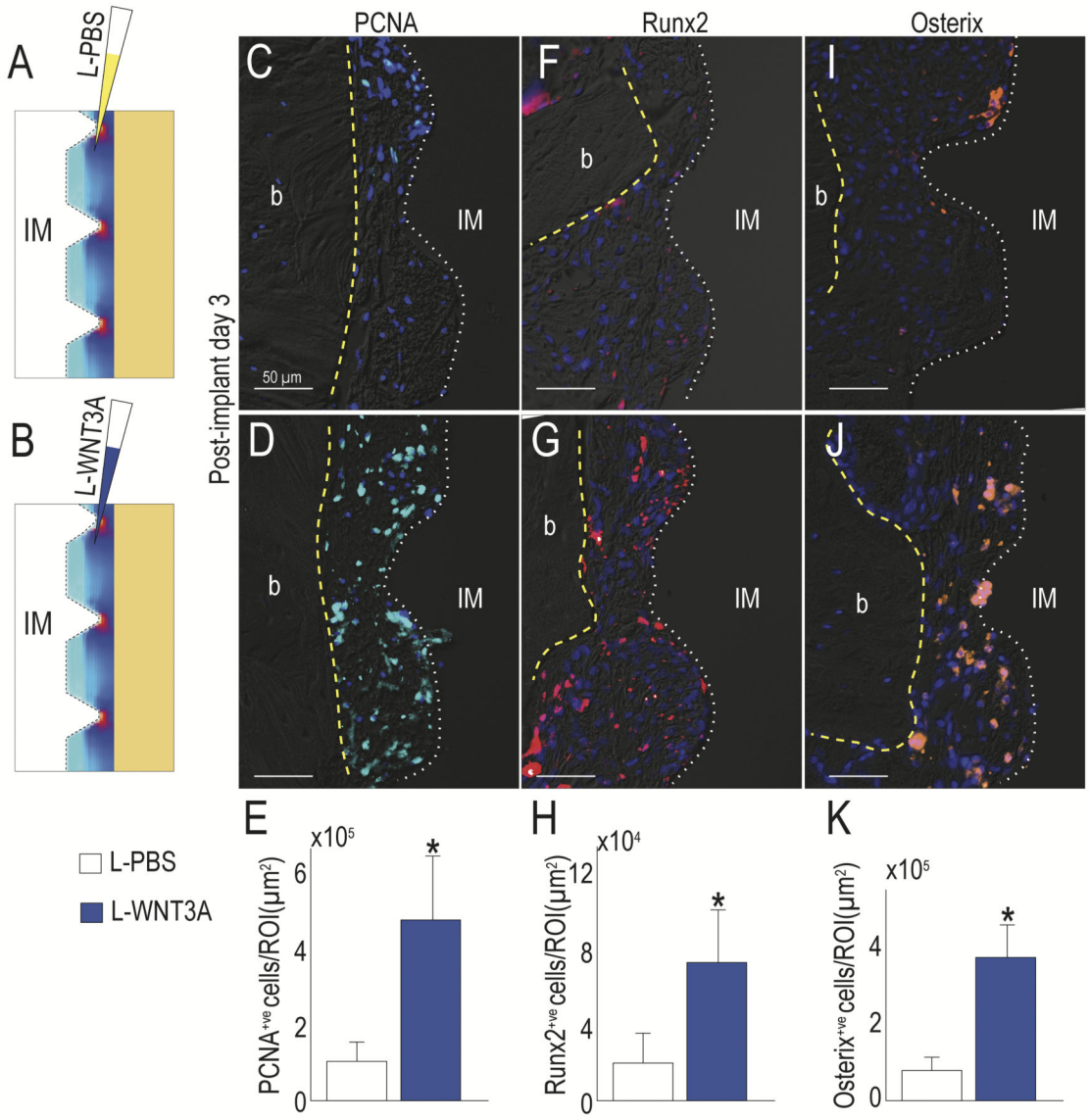

Fig. 2. L-WNT3A alters the fate of peri-implant cells towards an osteogenic lineage despite a high strain environment.

(A) Schematic of the experimental treatment, where L-PBS or (B) L-WNT3A were injected into the peri-implant environment, whose strain distribution is illustrated by a schematized heat map. PCNA expression in (C) control L-PBS vs (D) L-WNT3A treated groups was evaluated to detect proliferative cells (quantified in E), Runx2 expression in (F) control L-PBS vs (G) L-WNT3A treated groups (quantified in H) and Osterix expression in (I) control L-PBS vs (J) L-WNT3A treated groups (quantified in K) were evaluated to detect osteogenic differentiation. Abbreviations: b, bone; IM, implant. Scale bars = 50µm. Asterisk indicates $p<.05$.

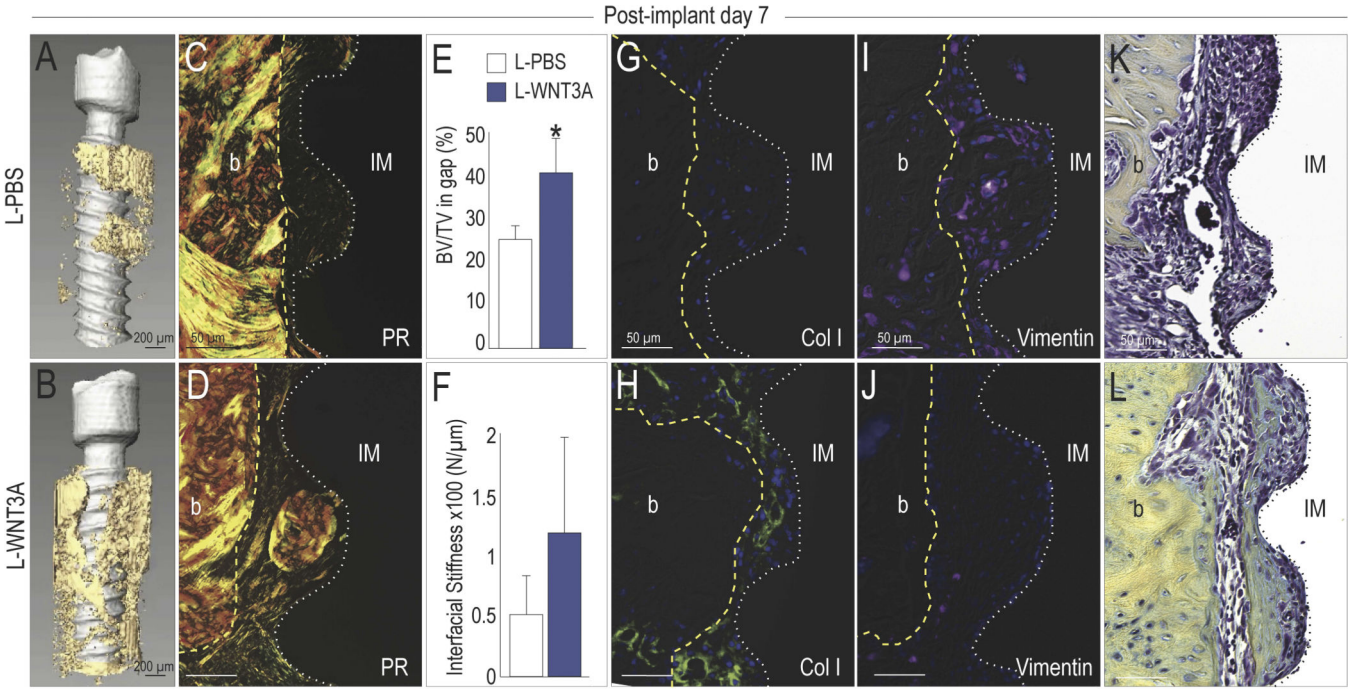

Fig. 3. L-WNT3A-induced peri-implant bone forms in regions of lower strains.

Representative 3D μCT imaging to assess peri-implant bone formation in cases treated with (A) L-PBS or (B) L-WNT3A. Sirius red staining observed with polarized light of representative sections from (C) L-PBS and (D) L-WNT3A. (E) Quantification of Bone Volume over Total Volume in the gap region. (F) Lateral stability testing of implants treated with L-PBS or L-WNT3A on PID7 (N=8, p=0.34). Collagen Type I expression observed in representative sections from (G) L-PBS and (H) L-WNT3A. Vimentin expression in representative sections from (I) L-PBS and (J) L-WNT3A. On PID7, Pentachrome staining of representative sagittal sections of (K) L-PBS and (L) L-WNT3A treated sites. Scale bars = 200μm (A, B), 50μm (G-L). Abbreviations: b, bone; IM, implant. Asterisk indicates p<.05.

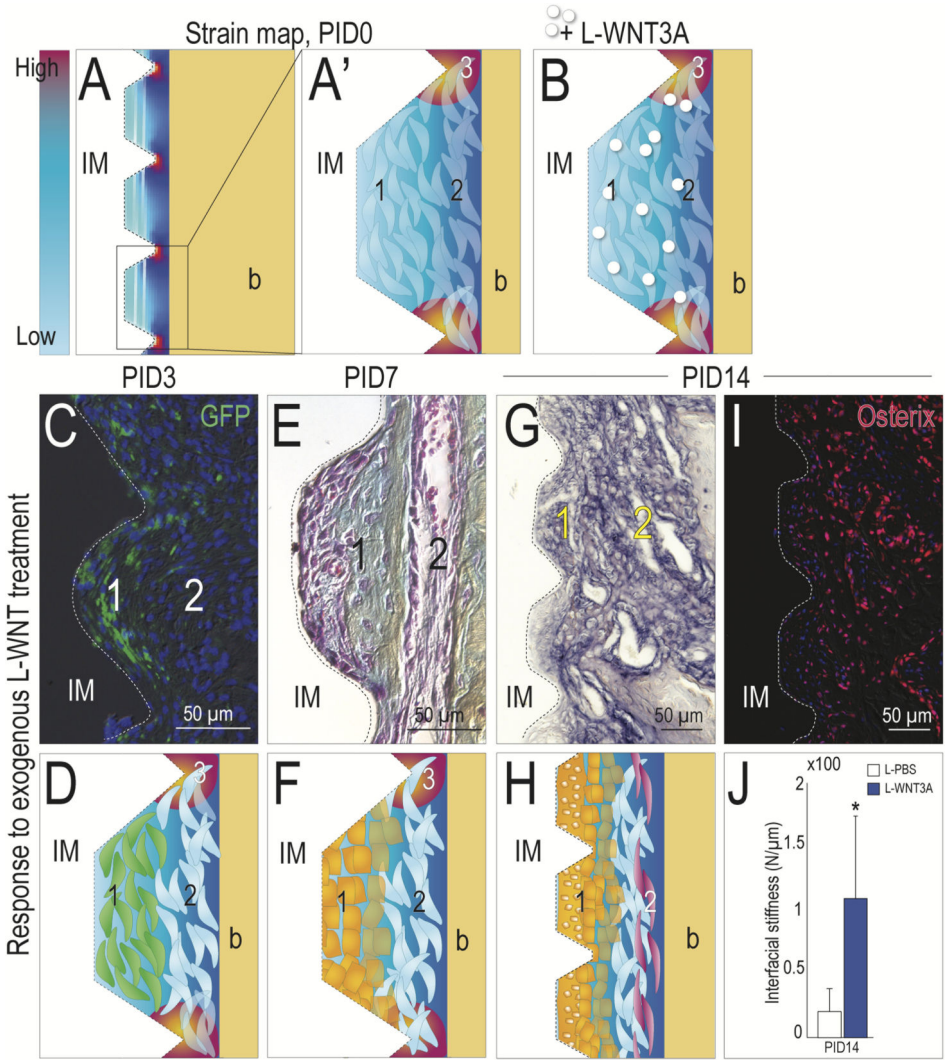

Fig. 4. Temporal and spatial progression of peri-implant osteogenesis triggered by L-WNT3A

(A,A') Strain map obtained from FE analyses, displaying a continuum of increasing strains, from Zone 1 (light blue, at the implant surface, between the threads) to Zone 3 (bright red, at the thread tips). (B) Illustration of L-WNT3A treatment at time of surgery where liposomes are evenly dispersed throughout the peri-implant blood clot. (C) GFP immunostaining for WNT responsive cells in $Axin2^{CreERT2/+}$;$R26R^{mTmG/+}$ mice; the majority of Wnt-responding cells are localized in the lower strain, Zone 1 region. These data are summarized in (D) an illustration depicting the distribution of WNT-responsive cells (green) and undifferentiated cells (light blue) 3 days after L-WNT3A treatment. (E) Pentachrome staining at PID7 assessed the state of ossification in Zone 1. (F) Illustration of cell activity at PID7 where osteoblasts (yellow squares) are confined to Zone 1 while the outer gap region remains fibrous (blue cells). (G) ALP activity in the peri-implant gap at PID14. (H) Illustration of tissue layers comprising the gap region at PID14. (I) Osterix IHC showing the strong osteogenic activity in the gap region at PID14. (J) Lateral stiffness testing of L-PBS

and L-WNT3A treated groups at PID14. Scale bars = 50μm (B, H). Abbreviations: b, bone; IM, implant. Asterisk indicates $p<.05$.

Table 1:

Experimental design

Experiment	Details
Species	*Rat rattus*, following OVX
Location of osteotomy	healed M1 extraction site
Type of bone	III
BV/TV of osteotomy (%)	60
pilot drill type	Drill Bit City
pilot drill size (mm)	0.33
final drill type	Drill Bit City
final drill diameter	0.65
L-PBS in a liquid collagen gel	
L-WNT3A in a liquid collagen gel	1.9 ng/μL active WNT3A
Implant inner diameter, ID (mm)	0.49
implant external diameter, ED (mm)	0.62
misfit between osteotomy diameter & implant external diameter, ED (mm)	0.65–0.62 = 0.03; therefore 0.015/side
misfit between osteotomy diameter & implant internal diameter, ED (mm)	0.65–0.49 = 0.16; therefore 0.08/side

Table 2

Preparation of collagen gel

Reagent (Concentration)	volume
Type I collagen (5mg/mL)	400 μL
H_2O	40 μL
10X Phosphate Buffer Saline	50 μL
1N NaOH	10 μL

Table 3:

Quantification of protein expression, peri-implant bone and interfacial stiffness

Variable	Day of analysis	L-PBS	L-WNT3A	p	Shown in
$PCNA^{+ve}$ cells/μm^2	PID3	$1.15\times10^{-5} \pm 4.8\times10^{-6}$	$5.24\times10^{-5} \pm 1.6\times10^{-5}$	0.0072	Fig. 2
$Runx2^{+ve}$ cells/μm^2	PID3	$2.26\times10^{-4} \pm 6.73\times10^{-5}$	$7.72\times10^{-4} \pm 2.3\times10^{-4}$	0.0291	Fig. 2
$Osterix^{+ve}$ cells/μm^2	PID3	$5.7\times10^{-6} \pm 5.06\times10^{-6}$	$3.86\times10^{-5} \pm 9.61\times10^{-6}$	0.0103	Fig. 2
Sample size		4	4		
Minimum required sample size		4	4		
BV/TV (%) in gap	PID7	25.6 ±6.5	45.2 ±10.2	0.0036	Fig. 3
Sample size		4	4		
Minimum required sample size		4	4		
Lateral stability test (N/μm)	PID7	$5.22\times10^{-3} \pm 3.14\times10^{-3}$	$11.9\times10^{-3} \pm 7.8\times10^{-3}$	0.342857	Figs. 3
Sample size		9	9		
Minimum required sample size		4	4		
Lateral stability test (N/μm)	PID14	$2.04\times10^{-3} \pm 0.8\times10^{-3}$	$10.62\times10^{-3} \pm 3.9\times10^{-3}$	0.029401	Fig. 4
Actual sample size		8	8		
Minimum required sample size		4	4		